Contents lists available at ScienceDirect

European Polymer Journal

journal homepage: www.elsevier.com/locate/europolj

Macromolecular Nanotechnology

Molecular dynamics simulations of the buckling behavior of defective carbon nanotubes embedded in epoxy nanocomposites

X. Peng, S.A. Meguid*

Mechanics and Aerospace Design Laboratory, Department of Mechanical and Industrial Engineering, University of Toronto, Toronto, Ontario M5S 3G8, Canada

ARTICLE INFO

Keywords:
Carbon nanotube
Defect
Buckling
Molecular dynamics
Nanocomposite
Epoxy

ABSTRACT

Many investigations have identified buckling of CNTs as a common mode of failure of CNT-reinforced nanocomposites. Several studies have also focused on the influence of defects on the buckling properties of freestanding CNTs. However, it is found that molecular dynamics (MD) based investigations concerned with the buckling of embedded CNTs are rare in the literature. In this research, the effects of various vacancy and Stone-Wales (SW) defect configurations on the buckling behavior of freestanding and embedded single-walled CNTs (SWCNTs) are investigated using MD. The simulations are based on the consistent valence forcefield (CVFF) and performed with the aid of LAMMPS. Our findings revealed different degradation effects and buckling modes for freestanding and embedded SWCNTs. The defects generally have the same influence on the buckling strain of the freestanding and embedded SWCNTs. However, it is found that increasing the number of missing atoms generally reduces the buckling load of freestanding SWCNTs, while increasing it for embedded armchair SWCNTs.

1. Introduction

Carbon nanotubes (CNT) have provoked considerable attention by the community since their discovery by Iijima [1], due to their promise and potential as reinforcements in polymer-based nanocomposites. Compared with traditional materials, advanced polymer nanocomposites possess superior multifunctional properties; including, much enhanced mechanical, electrical, and thermal properties [2]. They are used in lightweight automobile and aerospace engineering applications, molecular electronics, energy storage devices, and biomedical applications.

Considerable experimental and theoretical investigations had been conducted to characterize the interfacial shear strength (ISS) of CNT-reinforced nanocomposites. However, significant discrepancies exist between the experimental results and theoretical predictions. For example, Cooper et al. [3] carried out pull-out experiments using a scanning probe microscope. The measured ISS varied from 35 to 376 MPa for single-walled CNTs (SWCNTs) and multi-walled CNTs (MWCNTs) embedded in an epoxy matrix. Barber et al. [4] used an atomic force microscope (AFM) to conduct direct CNT pull-out experiments. The observed ISS was 47 MPa for MWCNTs embedded in a polyethylene-butene matrix. By contrast, Wagner et al. [5] combined fragmentation tests used Kelly-Tyson model to estimate the mechanical strength of CNT-urethane composite interface. The ISS was estimated to be on the order of 500 MPa and higher. Liu et al. [6] examined the effect of noncovalent and covalent functionalization on the interfacial properties of a SWCNT-epoxy system using molecular dynamics (MD) simulations. Their results revealed that the ISS can be increased by up to 940 MPa by properly designing hybrid systems containing both covalent and noncovalent functionalization. Xiong and Meguid [7] employed MD

* Corresponding author.
E-mail address: meguid@mie.utoronto.ca (S.A. Meguid).

http://dx.doi.org/10.1016/j.eurpolymj.2017.06.010
Received 21 March 2017; Received in revised form 28 May 2017; Accepted 3 June 2017

Available online 06 June 2017

simulations to investigate the interfacial mechanical characteristics of CNT-reinforced epoxy composites. The calculated ISS varied from 20 to 80 MPa for different SWCNT-epoxy systems. These theoretically obtained results differ dramatically from the experimental values. Scientists attributed this discrepancy to various anomalies in CNT-reinforced nanocomposites. The main anomalies include defects in CNTs such as vacancies and Stone-Wales (SW) as well as buckled CNTs in nanocomposites. These defects and deformed CNTs inevitably develop during their synthesis as well as manufacturing [8–11].

Due to their large aspect ratios and hollow cylindrical structure, CNTs are prone to buckle under compressive loads. Buckling can result in ultimate tube collapse in the form of an abrupt decline in the compressive load carrying capacity and undesirably distorted configuration of the considered structures. Under axial compression, a CNT may exhibit shell-like or beam-like buckling depending on its aspect ratio. Shell-like buckling occurs when the aspect ratio is relatively small, while beam-like buckling occurs when the aspect ratio is relatively large. Some experimental and theoretical studies have investigated the buckling behavior of CNT-reinforced nanocomposites. Experimental efforts have depicted CNTs in buckled state both as individual CNTs [12–14] and as embedded in nanocomposites [15,16]. A large volume of theoretical work, based on both continuum-based beam and shell principles [17–19], and atomistic techniques such as MD [20–24] concentrated on buckling of standalone nanotubes. However, an increasing number of researchers studied the compressive behavior of CNTs when embedded in nanocomposites. For instance, Lourie et al. [15] coupled the classical Euler model with an energy method to examine the CNT buckling behavior within a polymeric matrix. To study the influence of transverse shear deformation, Zhang et al. [25] developed Timoshenko beam model, which offers a more accurate estimate of the critical buckling stress. Based on the classical shell theory [26], Ru [27] established an elastic double-walled shell model for the buckling investigation of CNTs in an elastic matrix. Later, Liew and coworkers [28,29] introduced a Pasternak foundation into Ru's model [27]. They proposed multi-walled shell model to describe the buckling behavior of MWCNTs that are embedded in a matrix with consideration of the van der Waals (vdW) interactions.

Since CNTs are highly prone to structural defects and buckling, a few investigations have also focused on the buckling behavior of defective CNTs. For instance, Chandra and Namilae [30] conducted MD simulations to study the compressive behavior of SWCNTs with chemical functionalization and SW defects. Their results revealed that functionalization and topological defects have a negative impact on the buckling stress of CNTs. The compressive behavior of SWCNTs and double-walled CNTs in the presence of vacancy defects was further examined by Hao and coworkers [31,32] using MD simulations. They found that the extent to which vacancy defects weaken the compressive load carrying capacity of CNTs is dependent on the length, chirality, and temperature of the nanotubes as well as the density of the defects and their relative position. Zhang et al. [33] conducted MD investigation into the buckling behavior of SWCNTs with defects. They revealed that point defects lead to a higher reduction in the buckling load than SW defects. Kulathunga et al. [34] examined the influence of various patterns of vacancy defects on the buckling of SWCNTs by MD simulations under different thermal environments. Their findings revealed that increasing the number of missing atoms, asymmetry of vacancy configurations, and asymmetric distribution of vacancy groups led to an increased decline in buckling resistance of CNTs. Ranjbartoreh and Wang [35] studied the effects of radius, chirality, length, single vacancy defect, and SW defect on the buckling behavior of SWCNTs. Their results indicated that the axial stability of SWCNTs decreases dramatically as a result of topological defects and the critical buckling strain is more prone to defects than the critical buckling force. The effect of aspect ratios of defective CNTs on the buckling behavior of CNTs was also investigated by Parvaneh et al. [36], who showed that single vacancy defects only have a weak impact on the critical buckling load of CNTs with a large aspect ratio at room temperature. Poelma et al. [37] combined analytical continuum theory with MD to study the influence of vacancy defect position on the CNT critical buckling load. They concluded that at 1 K the critical buckling load and strain are dramatically reduced by the defects at the ends or close to the middle of the CNT. The compressive mechanical properties of SWCNTs with up to 20 randomly distributed vacancies were studied by Cheng et al. [38] using MD. They found that Young's modulus of the SWCNTs is approximately linearly proportional to the number of vacancies and that SWCNTs containing more vacancies have a more complex deformation pattern.

However, it is evident from the preceding literature review that there has been no work on the influence of various defects on the buckling of embedded CNTs. To the authors' knowledge, only a few studies have used MD simulations to study the buckling of embedded pristine CNTs. For instance, Namilae and Chandra [39] studied the compressive behavior of CNTs embedded in polyethylene (PE) matrix using MD simulations. They found that the buckling load increases only very slightly for CNTs embedded in PE matrix compared with neat nanotubes. In the case of chemically bonded interfaces, the critical buckling stress is decreased compared with the pristine CNTs due to the variations in curvature introduced by chemical bonding. The buckling of SWCNTs embedded in PE matrix was examined by Kulathunga and Ang [40]. They found that the embedded CNT has higher buckling stress compared to the freestanding CNT. It is clear from the above that there exists a need to conduct a comprehensive investigation on the buckling of defective CNTs embedded in polymer nanocomposites.

The objective of this paper is to study the influence of vacancy and SW defects on the buckling behavior of CNTs embedded in an epoxy matrix. Defects with different densities and configurations were modeled. The MD simulations were performed at room temperature (300 K) by means of the consistent valence forcefield (CVFF). To tackle the chirality influence, we considered armchair and zigzag SWCNTs with similar diameters. During the compressive loading process, the majority of the epoxy matrix surrounding the CNT was allowed to deform freely to capture the influence of matrix deformation on the buckling of the embedded CNTs accurately.

2. Molecular modeling

Large-scale atomic/molecular massively parallel simulator (LAMMPS) [41] were employed to conduct all MD simulations. It is very important to choose an appropriate interatomic potential that has the ability to model complex systems under dynamic loading

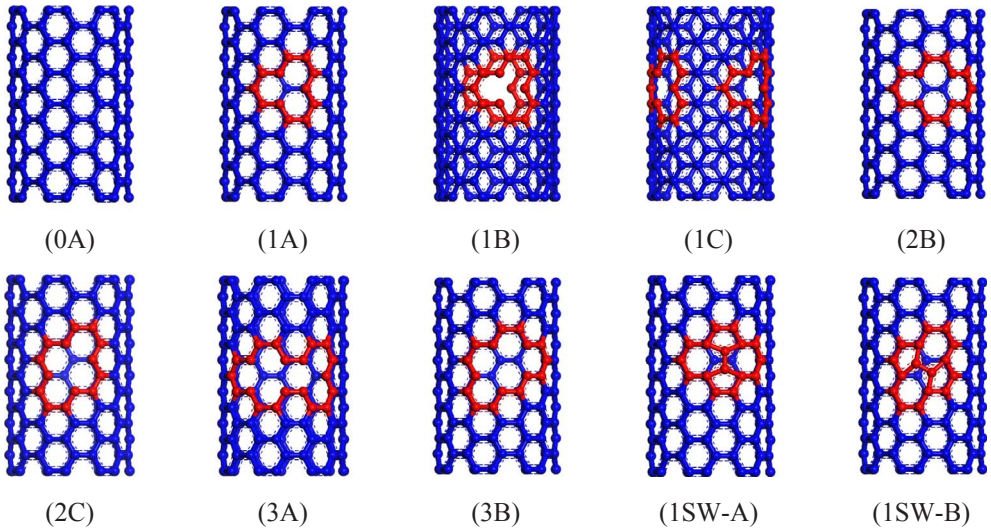

Fig. 1. Defects considered in this research (0A – pristine, 1A – monovacancy, 1B –two monovacancies symmetrically distributed, 1C – two monovacancies asymmetrically distributed, 2B – symmetric bivacancy, 2C – asymmetric bivacancy, 3A – symmetric trivacancy, 3B – asymmetric trivacancy, 1SW-A – symmetric SW defect, 1SW-B – asymmetric SW defect).

conditions accurately. In this study, all non-bonded and bonded interactions in the simulations were modeled using the CVFF [42]. This force field has been widely adopted by other scientists to investigate the mechanical properties of CNT-reinforced epoxy composites [43–46].

2.1. Molecular structure of CNTs with defects

It is expected that defects have an influence on the buckling behavior of CNTs, since buckling is very sensitive to geometric imperfections. However, it is crucial to understand the role played by the different defects on the buckling behavior of nanotubes. For example, a number of factors influence the buckling behavior of CNTs containing vacancies and SW defects. For instance, the number and location of these defects, the number of vacancy clusters and their distribution govern the buckling behavior of CNTs. In order to examine the impact of these factors, the defect patterns given in Fig. 1 were investigated. As shown in Fig. 1, one, two and three-bonded carbon atoms were removed from the pristine SWCNT to form the monovacancy, bivacancy, and trivacancy, respectively. The SW defect displayed in Fig. 1 was developed via a 90° rotation of the carbon-carbon bond, converting four hexagons into two heptagons and pentagons (5-7-7-5). Specifically, vacancies coded (1A), (2B), and (3A) are symmetric monovacancy, bivacancy, and trivacancy, respectively. Vacancies coded (2C) and (2B) are asymmetric bivacancy and trivacancy, respectively. Both vacancies coded (1B) and (1C) have two monovacancies. The monovacancy (1B) is located exactly opposite to each other, while the monovacancy (1C) is located close to one side of the CNTs. Symmetric and asymmetric SW defects are coded (1SW-A) and (1SW-B), respectively. Armchair (7, 7), (9, 9) and zigzag (12, 0) SWCNTs with the same aspect ratios of 6.5 were considered here. All defects were assumed to form at the sidewalls of SWCNTs. The defects were introduced at or near the middle of the nanotubes since defects at the mid-length are assumed to cause maximum reduction of the buckling load and the buckling strain [36,47].

2.2. Construction of freestanding CNT and nanocomposite RVE

It should be stressed that the current investigation is concerned with the buckling behavior of an embedded CNT within a matrix and not the buckling behavior of the CNT-reinforced nanocomposites. Thus, both freestanding CNTs and CNT-epoxy nanocomposites were prepared here with the view to determine the influence of the surrounding matrix on the buckling behavior of defective CNTs. To prepare freestanding armchair (7, 7), (9, 9) and zigzag (12, 0) SWCNTs for compression, the total potential energy of the SWCNTs were initially minimized using the conjugate gradient method. This was followed by NVT equilibration at 300 K for 50 ps using a time step of 1 fs. The boundary condition was kept non-periodic in all three directions, and vdW interactions were truncated at a cutoff distance of 12 Å.

In order to carry out the buckling simulation of a CNT embedded in an epoxy matrix, we constructed a representative volume element (RVE) by incorporating a SWCNT embedded at the center of the RVE and the epoxy molecules. By employing a specific two-component epoxy resin based on a triethylene tetramine (TETA) curing agent and diglycidyl ether of bisphenol A (DGEBA) epoxy, we modeled the epoxy matrix system which is typically utilized in the aerospace industry. The epoxy system was created during the curing process by developing covalent bonds between the epoxide groups of the epoxy and the hydrogen atoms in the amine groups of the curing agent. Each epoxy oligomer includes four DGEBA molecules joined by one TETA molecule (refer to Fig. 2) so that a ratio of 100:16.7 is achieved for the resin-hardener weight in the epoxy polymer. Finally, Packmol software [48] were used to pack a number of epoxy oligomers into the RVE to obtain an appropriate density, and the final structure of the RVE is visualized by VMD [49] as

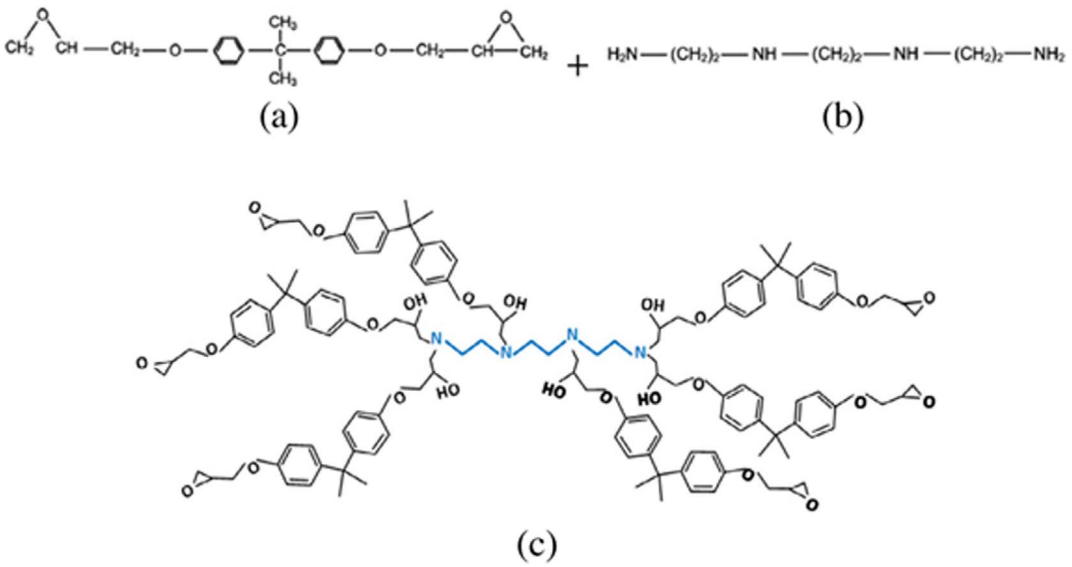

Fig. 2. Chemical configurations of (a) epoxy resin (DGEBA), (b) curing agent (TETA), and (c) cured epoxy oligomer (6 DGEBA molecules joined by 1 TETA).

displayed in Fig. 3(a). In this MD simulation, periodic boundary conditions were applied in x- and y-directions, while periodicity is removed in z-direction. The time step used in the MD simulation was 1 fs, and a cutoff distance of 12 Å was employed to model vdW interactions. The same parameters were followed for different RVEs containing different armchair (7, 7), (9, 9) and zigzag (12, 0) SWCNTs. For example, the key steps involved in preparing the buckling simulation for the (7, 7) pristine SWCNT-epoxy nanocomposites are as follows:

Step 1 – Volume reduction: Due to the presence of rigid molecules in the Packmol software, the RVE was initially expanded to accommodate all the epoxy molecules and the CNT atoms. Next, the appropriate density of the RVE was achieved by gradually compressing the RVE through seven steps from its original dimensions of 150 Å × 150 Å × 62 Å to the final size of 50 Å × 50 Å × 62 Å. At each phase, the CNT was "frozen", and the coordinates of the epoxy atoms were remapped to fit inside the compressed box. The conjugate gradient method was then utilized to minimize the potential energy of the compressed box. The final compressed box is shown in Fig. 3(b).

Step 2 – Equilibration: Nose-Hoover algorithm was initially used to distribute the molecules evenly due to the volume reduction by equilibrating the compressed box for 2 ns in the isothermal-isobaric (NPT) ensemble at 300 K and 1 atm. The following temperature cycle protocol was used to ensure equilibrium. We performed two stepwise NPT cycles of heating and cooling (from 400 K to 300 K by a step of 25 K) with each step occupying 10 ps. Subsequently, the epoxy system was simulated in the NPT ensemble for 1 ns at 300 K and 1 atm to create appropriate CNT-matrix interfacial thickness. The final equilibrated density of the SWCNT-epoxy RVE was found to be 0.95 g/cm^3, which is slightly less than expected because of the non-periodic boundary in the z-direction of the RVE.

2.3. Compression test

The MD compression simulations were conducted to determine the critical buckling strain and buckling load of both freestanding

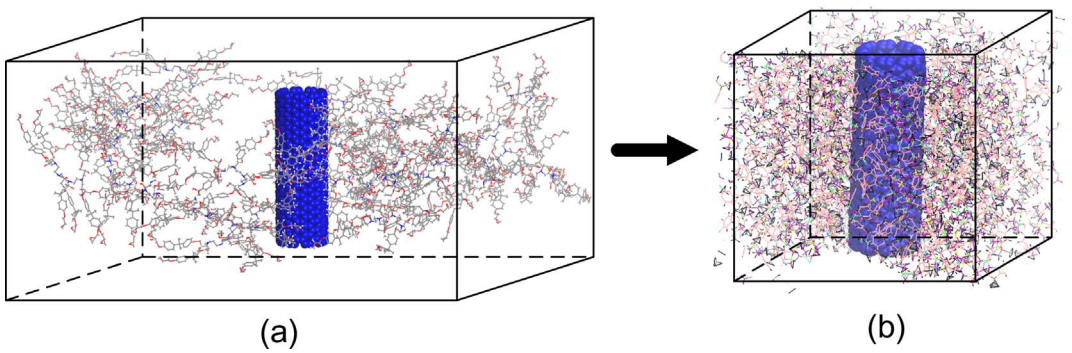

Fig. 3. Preparation of the RVE (a) SWCNT embedded in randomly placed cured epoxy oligomers, and (b) the compressed SWCNT-epoxy system.

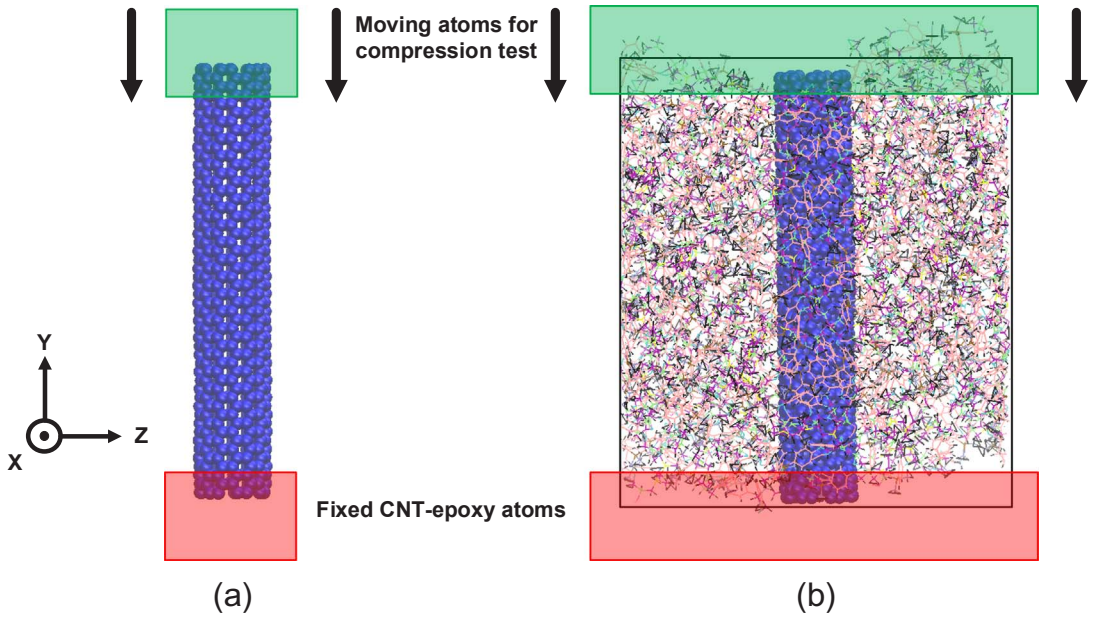

Fig. 4. Setup for the buckling simulations of (a) freestanding SWCNT, and (b) SWCNT embedded in the epoxy matrix.

SWCNTs and SWCNT embedded in epoxy nanocomposite systems. To prevent the simultaneous drift of the SWCNT and epoxy atoms in the z-direction during the compression process, we constrained one end of the freestanding SWCNT and the RVE (shown in red in Fig. 4). In order to avoid the effect of the constraint on the final results, the constrained systems were further equilibrated in the NVT ensemble at 300 K for 50 ps. The composition of the freestanding SWCNTs and RVEs containing different SWCNTs prior to the compression process is listed in Table 1. After the equilibration was complete, an incremental displacement loading of 0.01 Å was applied on the other end of the freestanding SWCNTs and the RVEs, which are marked in green in Fig. 4. After each increment, the systems were relaxed for a period to achieve a new equilibrium state while maintaining the two ends constrained. The loading was repeated at 300 K in the NVT ensemble until the buckling occurred. During the compression process of the RVE, both the SWCNT and surrounding epoxy atoms were applied an axial load in the z-direction. Since the interactive deformation of the CNT and the epoxy atoms were enabled, our method can capture the effect of each defect accurately on the buckling behavior of CNTs embedded in a deformable epoxy polymer matrix.

2.4. Evaluation of buckling behavior

As for the assessment of the buckling behavior, the strain energy curves and force-displacement curves for the armchair (7, 7), (9, 9) and zigzag (12, 0) pristine SWCNTs are displayed in Fig. 5(a) and (b), respectively. The critical buckling state is detected by an abrupt drop in the strain energy or the force. This sudden drop is associated with significant structural and geometrical changes of CNTs (as shown in Fig. 6) corresponding to the release of energy of CNTs. It can be seen in Fig. 6 that different pristine SWCNTs with an aspect ratio of 6.5 buckle sideways with the occurrence of a flattening at the center, which is recognized in the literature as being "beam-shell buckling mode". It is a mixture of globalized beam-like buckling for a long and slender CNT and localized shell-like buckling within the atomic layer of a short CNT. In agreement with the findings of Wang et al. [24,50], we conclude that CNTs with aspect ratios more than 6, exhibit beam-shell buckling mode, while preserving its circular cross section with localized shell buckling within the atomic layer. It is further observed from Fig. 5(a) that the strain energy can be approximately expressed as a quadric function of the strain before the singularity occurs in each curve, viz;

Table 1
Composition of freestanding SWCNTs and RVEs containing different SWCNTs immediately before compression simulations.

SWCNT			Epoxy	Composites				
Chiral vector	Length (Å)	Radius (Å)	No. of chain	X (Å)	Y (Å)	Z (Å)	Density (g/cm^3)	Total number of atoms
(7, 7)	55.89	4.46	–	–	–	–	–	700
(9, 9)	72.11	5.73	–	–	–	–	–	1152
(12, 0)	56.68	4.39	–	–	–	–	–	696
(7, 7)	55.47	4.48	44	52.47	52.47	66.79	0.95	14868
(9, 9)	71.70	5.75	57	52.21	52.21	87.05	0.97	19506
(12, 0)	55.97	4.45	44	52.47	52.47	67.12	0.94	14864

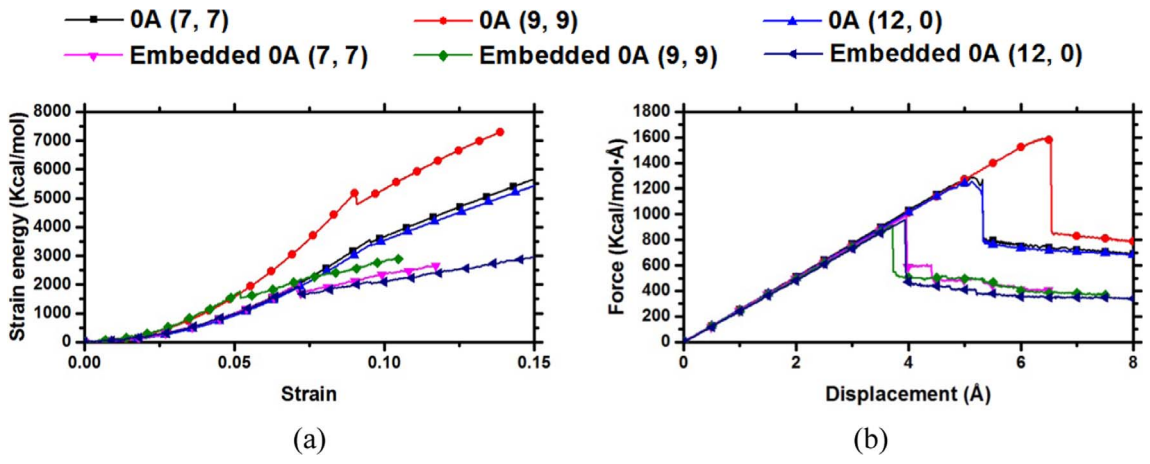

Fig. 5. (a) Strain energy-strain curves; (b) force-displacement curves for different pristine freestanding and embedded SWCNTs.

$$U = \frac{1}{2}EAL\varepsilon^2 \tag{1}$$

where U, E, A, L, and ε are the strain energy, Young's modulus, cross-sectional area, original length, and strain of the nanotubes, respectively. This indicates that the SWCNTs sustain elastic deformation under a compressive force in accordance with Hooke's law until bifurcation. Note that in Fig. 5(a), the critical buckling strain is defined as the strain at which the strain energy of the simulated SWCNT displays its first abrupt drop in value. We can also see in Fig. 5(b) that the compressive force which the SWCNTs can withstand increases almost linearly with the axial displacement until the buckling load is reached, such that,

$$F = \frac{EA}{L}\Delta L \tag{2}$$

where F is the compressive force and ΔL is the end-shortening displacement. In Fig. 5(b), the critical buckling load P_{cr} is the upper value of the axial load P at the critical buckling state, and the corresponding displacement is the critical end-shortening Δ_{cr}. After buckling, the CNT enters into the postbuckling stage. In the postbuckling stage of bifurcation, the pronounced bending effects lead to more severe distortion of the CNTs, resulting in a decrease in the compressive force. Coincident with the value obtained from the strain energy, the critical buckling strain ε_{cr} can also be calculated by dividing Δ_{cr} by the original length L of CNT. Furthermore, according to Eq. (2), the slope of the load-displacement curve is an indicator of Young's modulus of CNTs.

3. Results and discussions

3.1. Effect of vacancy defects on freestanding SWCNTs

This section focuses on exploring the effect of different vacancy defects on the buckling behavior of freestanding SWCNTs. Based on the foregoing definitions of Section 2.4, the buckling strain and the buckling load of the investigated cases are provided in Table 2. We can see that the armchair SWCNT (7, 7) possesses very similar buckling capacity compared to the zigzag SWCNT (12, 0) with the same length and diameter. However, the buckling strain of the armchair SWCNT (9, 9) is smaller than that of the armchair SWCNT (7, 7) with the same aspect ratio. The reverse is observed when the buckling load is considered. Our results are consistent with those reported by other researchers for the free standing CNT studies. For instance, Wang et al. [24] used MD simulations to study a wide range of armchair SWCNTs based on AIREBO potential. Their results revealed that the buckling strain is in the range of 0.0131 to 0.0734 and the buckling load varies from 18.6 nN to 86.8 nN. Zhang and coworkers [50,51] also found that the nonlocal cylindrical shell model predicts comparable results for SWCNTs with short aspect ratios ($L/d < 8$). The buckling strain can reach up to 0.1 when the aspect ratio is close to 5. Zhang et al. [52] investigated the effect of chirality on the buckling behavior of SWCNTs. They reported that the influence of chirality can be neglected for SWCNTs with relatively larger chiral angles.

Next, we turn our attention to the effect of vacancy defects on the buckling behavior of freestanding CNTs. Fig. 7 shows the strain energy versus strain and the force-displacement curves for armchair (7, 7), (9, 9) and zigzag (12, 0) defective SWCNTs. The buckling strain and buckling load obtained, depicted in Fig. 7, are compared with the pristine SWCNTs and listed in Table 2. The buckling modes of the different defective SWCNTs are shown in Fig. 6. It is interesting to observe from Fig. 6 that the buckling modes of the different defective SWCNTs are similar to that of the pristine SWCNTs, where one flattening is formed at the center. In order to investigate the influence of missing atoms, only the symmetric vacancies (1A), (2B), and (3A) are analyzed here. Based on the slopes of the load-displacement curves, and as expected, Young's modulus decreases with the increase in the number of missing atoms. It can also be seen from the results that the monovacancy (1A) has the lowest buckling strain, but increasing the number of missing atoms decreases the buckling load irrespective of the chirality of SWCNTs. It is easy to understand that monovacancy is superior to bi-vacancy and trivacancy because the defective area induced by the monovacancy is obviously smaller. However, by taking a closer

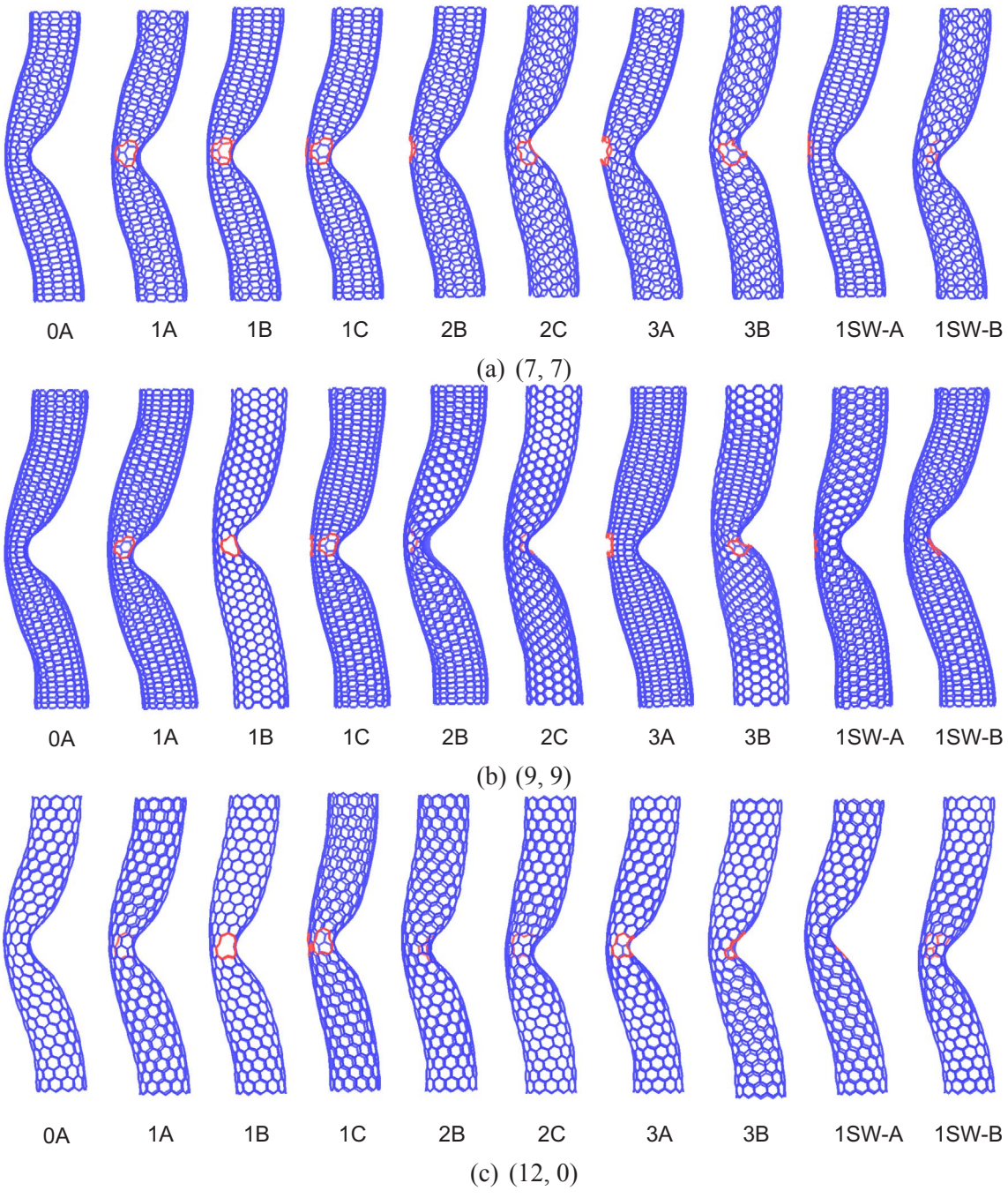

Fig. 6. Buckling mode shapes of the freestanding SWCNTs (a) (7, 7), (b) (9, 9) and (c) (12, 0).

look at the buckling shapes in Fig. 6, monovacancy tends to cause the edge of buckled flattening close to the defect, leading to excessive stress concentration. This makes the local buckling takes place more readily at the defective position.

The vacancies (2B), (2C), (3A), and (3B) are considered next to study the effect of symmetric and asymmetric configurations on the buckling behavior. According to the slopes in the load-displacement curves, the presence of asymmetric vacancies reduces Young's modulus. Furthermore, for armchair SWCNTs, the results of Fig. 7 and Table 1 show that asymmetric vacancies, compared with symmetric counterparts, cause a higher decline in the buckling strain but not in the buckling load. This can be explained with the aid of Fig. 6 which shows that asymmetric vacancies develop flattening kinks near the defect, which expedites buckling instability. Those kinks serve to withstand more loads and increase the buckling load. However, a difference can be observed between armchair and zigzag SWCNTs. For zigzag SWCNTs, asymmetric vacancies reduce both the buckling load and the buckling strain, and the buckling behavior is more affected by trivacancies. This may be due to the special bond structure of zigzag CNTs.

Table 2
Comparison of buckling behavior of freestanding defective SWCNTs with the buckling behavior of freestanding pristine SWCNTs.

CNT type	CNT configuration	Buckling strain	% reduction w.r.t. pristine CNT	Buckling load (kcal/mol-Å)	% reduction w.r.t. pristine CNT
(7, 7)	0A	0.095		1276 (89 nN)	
	1A	0.091	4.3	1208	5.3
	1B	0.084	11.3	1178	7.7
	1C	0.090	5.0	1140	10.7
	2B	0.094	0.7	1134	11.1
	2C	0.090	5.8	1215	4.8
	3A	0.092	3.0	1094	14.2
	3B	0.085	10.2	1145	10.2
	1SW-A	0.093	2.5	1130	11.5
	1SW-B	0.092	3.5	1224	4.0
(9, 9)	0A	0.091		1560 (108 nN)	
	1A	0.086	4.7	1520	2.6
	1B	0.086	5.4	1575	-0.9
	1C	0.087	4.3	1566	-0.3
	2B	0.089	1.6	1513	3.0
	2C	0.087	3.7	1543	1.1
	3A	0.087	4.2	1418	9.1
	3B	0.086	4.8	1556	0.3
	1SW-A	0.085	6.3	1489	4.6
	1SW-B	0.089	1.4	1506	3.5
(12, 0)	0A	0.094		1222 (85 nN)	
	1A	0.090	4.6	1199	1.8
	1B	0.083	11.7	1148	6.0
	1C	0.087	7.3	1104	9.7
	2B	0.090	4.3	1163	4.8
	2C	0.091	3.6	1174	3.9
	3A	0.093	0.8	1122	8.2
	3B	0.085	9.7	1117	8.6
	1SW-A	0.097	-3.1	1021	16.4
	1SW-B	0.091	3.3	1138	6.8

The third focus here is on the influence of vacancy distribution on the buckling behavior of CNTs. Therefore, we studied SWCNTs containing vacancies (1B) and (1C). The results of Table 3 indicate that vacancy (1B) has lower buckling strain but higher buckling load than vacancy (1C). This again occurs as a result of the positions of kinks relative to the defects, as depicted in Fig. 6. Since the monovacancies in (1B) are located exactly opposite to each other, the kinks tend to form close to the defects, leading to excessive stress concentration. This makes vacancy (1B) easier to buckle than vacancy (1C), but allows vacancy (1B) to withstand higher loads for both armchair and zigzag SWCNTs.

3.2. Effect of missing atoms on embedded SWCNTs

In this section, we examine the effect of missing atoms on the buckling behavior of SWCNTs embedded in the epoxy matrix. Embedded pristine SWCNTs are firstly taken as a reference to compare with freestanding pristine SWCNTs alone. Fig. 5(a) and (b) shows the strain energy-strain and the force-displacement curves for the embedded pristine SWCNTs in comparison with pristine stand-alone SWCNTs. It is apparent from the slopes of the load-displacement curves that surrounding epoxy matrix does not have a major influence on the Young's modulus of embedded CNTs. Table 3 shows the buckling strain and buckling load obtained from Fig. 5. Interestingly, the surrounding epoxy matrix significantly reduces the resistance to the buckling of SWCNTs by up to 43%. The reason for the embedded CNTs to have lower resistance to buckling than the freestanding nanotubes is the uneven atomic forces exerted by the surrounding matrix atoms. These atomic forces deform the CNTs unevenly, leading to the easier occurrence of buckling. The buckled shapes in Fig. 8 show that the embedded pristine CNT displays only pure shell-like buckling modes, where two flattenings referred to as "fins" by Yakobson et al. [17], that are perpendicular to each other, are developed. This is because the atomic forces exerted by the surrounding matrix atoms provide some form of confinement, preventing the CNTs from buckling sideway. The buckling shape transformation may also lead to the decrease in the buckling strain and buckling load.

We now proceed to investigate the buckling of CNTs with different missing atoms (1A), (2B), and (3A) embedded in the epoxy matrix. Fig. 9 shows the strain energy-strain and the load-displacement plots for the defective embedded nanotubes discussed above. According to the slopes in the load-displacement curves, Young's modulus decreases with the increase in the number of the missing atoms. As demonstrated in Table 3, both the buckling strain and the buckling load are higher when compared with the embedded pristine armchair SWCNTs, as the number of missing atoms increases. The maximum reductions in the buckling strain and buckling load are 29% and 31%, respectively. This is also higher than what we observed in freestanding defective armchair SWCNTs. This may be explained by the buckled shapes depicted in Fig. 8. The first buckling mode occurs only on one side of the SWCNTs close to the missing atoms, which are neither beam-like nor shell-like buckling modes. These buckled modes depicted in Fig. 8 result in excessive

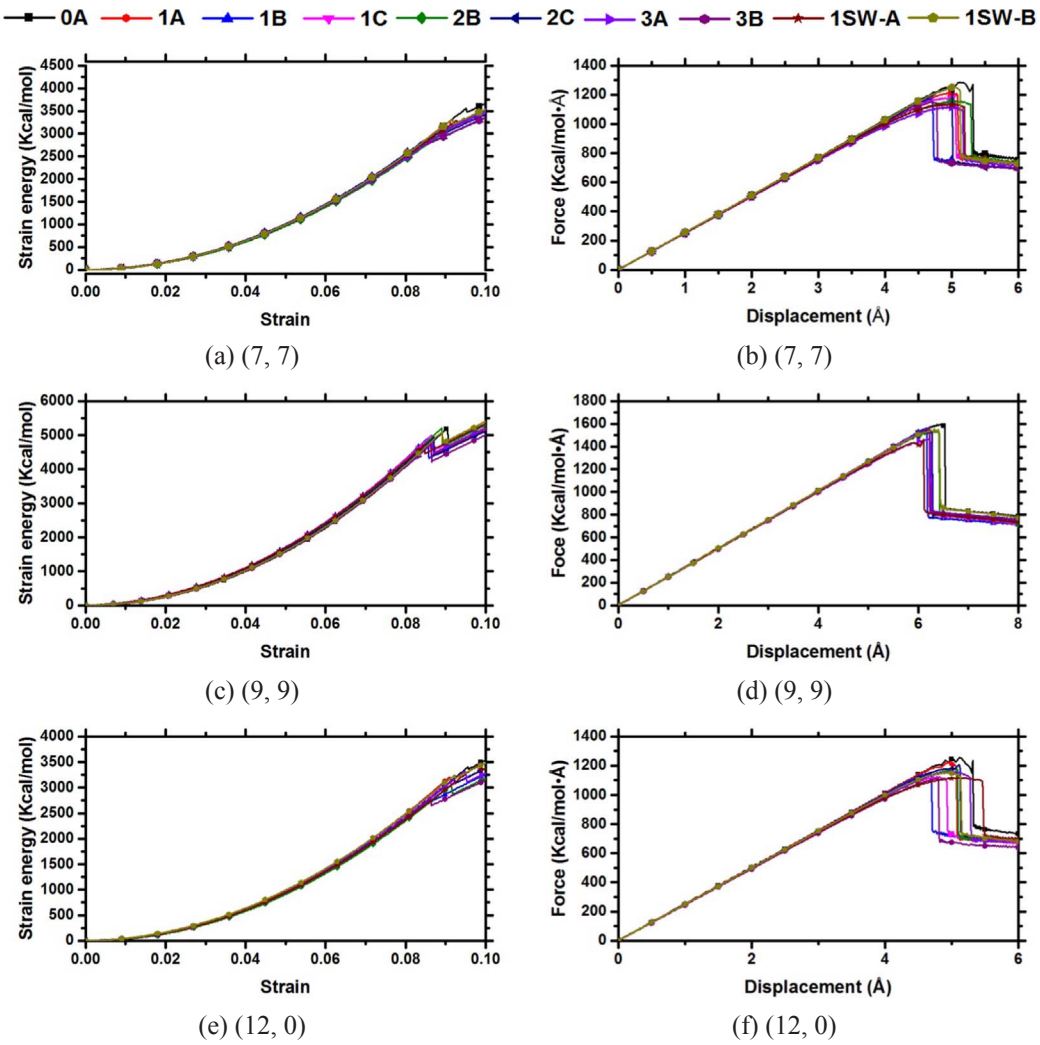

Fig. 7. (a), (c) and (e) Strain energy-strain curves; (b), (d) and (f) force-displacement curves for different freestanding defective SWCNTs.

stress concentration for the case involving monovacancies, leading to a minima of both the buckling strain and the buckling load. A closer look at the buckled shape of (3A) reveals that it displays a shell-like buckling mode due to its longer nanotube. This may contribute to a reduction in the buckling load. In contrast to the embedded defective armchair SWCNTs, Table 3 shows that both the buckling strain and buckling load of the embedded defective zigzag SWCNTs decrease with the increase in the number of missing atoms. This reveals that the increase in the number of missing atoms in zigzag SWCNTs has a more negative influence on the buckling behavior despite similar buckling shapes to the embedded defective armchair SWCNTs.

3.3. Effect of vacancy symmetry and distribution on embedded SWCNTs

First, let us focus our attention to the effect of symmetric and asymmetric vacancy configurations (2B), (2C), (3A) and (3B) on the buckling behavior of embedded SWCNTs. Analogous to freestanding SWCNTs and in accordance with the slopes of load-displacement curves of Fig. 9, asymmetric vacancies lead to an increase in Young's modulus compared with embedded nanotubes with symmetric vacancies, irrespective of the chirality of SWCNTs. This is similar to their freestanding counterparts. For the buckling strain and buckling load, we can see in Table 3 that asymmetric vacancies generally reduce the buckling behavior of both armchair and zigzag SWCNTs when compared with symmetric vacancies. This is different from the corresponding freestanding armchair nanotubes, where the buckling load is increased due to the presence of kinks in the asymmetric vacancies. Compared with the symmetric vacancies, asymmetric vacancies further reduce the buckling strain and buckling load by 5–20%, respectively. The reason for the discrepancy could be attributed to the fact that embedded defective SWCNTs display different buckling modes (Fig. 8), where the nanotubes only narrows at one side, while keeping their cylindrical shapes intact at the other side. The position of the narrowing is close to the existing vacancies. However, due to the longer length in (9, 9) nanotubes, the buckling behavior of bivacancies (2B) and (2C) is comparable. They tend to buckle in a shell-like manner similar to the embedded pristine SWCNTs.

Table 3
Comparison of buckling behavior of embedded defective SWCNTs with the buckling behavior of embedded pristine SWCNTs.

Embedded CNT type	CNT configuration	Buckling strain	% reduction w.r.t. pristine CNT	Buckling load (kcal/mol-Å)	% reduction w.r.t. pristine CNT
(7, 7)	0A	0.071		979 (68 nN)	
	1A	0.051	28.9	710	27.5
	1B	0.050	30.0	676	30.9
	1C	0.053	25.0	629	35.7
	2B	0.054	24.4	712	27.3
	2C	0.047	34.5	629	35.7
	3A	0.057	20.1	756	22.7
	3B	0.043	40.2	576	41.2
	1SW-A	0.059	17.0	784	19.9
	1SW-B	0.052	27.4	690	29.6
(9, 9)	0A	0.052		912 (63 nN)	
	1A	0.043	18.4	733	19.6
	1B	0.042	19.4	733	19.6
	1C	0.049	7.3	768	15.8
	2B	0.044	15.9	771	15.4
	2C	0.045	15.1	762	16.4
	3A	0.044	15.5	631	30.8
	3B	0.043	17.9	722	20.8
	1SW-A	0.048	7.6	866	5.1
	1SW-B	0.042	19.5	749	17.9
(12, 0)	0A	0.070		959 (67 nN)	
	1A	0.053	24.9	711	25.9
	1B	0.042	39.7	564	41.2
	1C	0.053	24.1	680	29.1
	2B	0.052	25.9	678	29.3
	2C	0.049	30.6	614	36.0
	3A	0.052	26.2	656	31.6
	3B	0.046	35.1	605	36.9
	1SW-A	0.056	20.7	750	21.8
	1SW-B	0.051	26.9	699	27.2

Second, let us devote our attention to the effect of vacancy distribution (1B) and (1C) on the buckling behavior of embedded SWCNTs. It is found (Fig. 9) that the embedded SWCNT with vacancy (1C) has a slightly lower Young's modulus than the one with vacancy (1B). This buckling behavior is similar to that observed in freestanding SWCNTs. This is a plausible observation as the asymmetric vacancy (1C) possibly reduces the stiffness of the nanotubes. Unlike the case of freestanding SWCNTs, both the buckling strain and buckling load of the SWCNTs containing the vacancy (1C) are increased (see Table 3) when compared with those of the SWCNTs containing the vacancy (1B), irrespective of the chirality of SWCNTs. This may be due to the different buckling modes present in Fig. 8, which are similar to the previously investigated embedded SWCNTs. It is worth noting that there exists an anomaly in the buckling load of (7, 7) SWCNT containing vacancy (1C). It is clear from Fig. 9(b) that (7, 7) SWCNT with vacancy (1C) does not show an abrupt drop in the load-displacement curve. We can see that the vacancy (1C) in (7, 7) SWCNT helps to delay the occurrence of buckling, leading to an increase in the buckling strain, although the buckling load remains relatively low.

3.4. Effect of SW defects on freestanding and embedded SWCNTs

Fig. 7 shows that the defective SWCNTs (1SW-B) generally possess higher Young's modulus than their counterparts (1SW-A) for both armchair and zigzag freestanding SWCNTs. This is similar to other freestanding symmetric and asymmetric SWCNTs. As shown in Table 2, the SW defects reduce the buckling capacity of SWCNTs in general. It is noted in Fig. 6 that kinks tend to develop close to the asymmetric SW defect (1SW-B). This leads to excessive stress concentration, which in turn expedites the occurrence of the buckling, and the kinks help to withstand more loads, leading to an increase in the buckling load.

In the second part of this section, we examine the influence of SW defects (1SW-A) and (1SW-B) of embedded SWCNTs on their buckling behavior. Based on the slopes of load-displacement depicted in Fig. 9, the embedded SW defective SWCNTs tend to have similar Young's moduli to the embedded pristine SWCNTs, which is different from their freestanding counterparts. This may be the result of the confinement provided by the surrounding matrix atoms. The embedded SWCNTs containing asymmetric SW defects (1SW-B) display lower buckling strain and buckling load (see Table 3) regardless of the chirality of SWCNTs. The maximum decreases in the buckling strain and buckling load are 22% and 30%, respectively, which are higher than the reduction found in their freestanding counterparts. The buckling modes for the embedded SW defective SWCNTs are similar to other embedded SWCNTs. Moreover, if we compare the buckling behavior of SW defective SWCNTs with vacancy defective SWCNTs in Table 3, it is apparent that the SW defects (1SW-A) have the least effect on the buckling behavior of embedded SWCNTs. By contrast, the degradation effect of embedded SW defective SWCNTs (1SW-B) is very similar to the corresponding embedded vacancy defective SWCNTs.

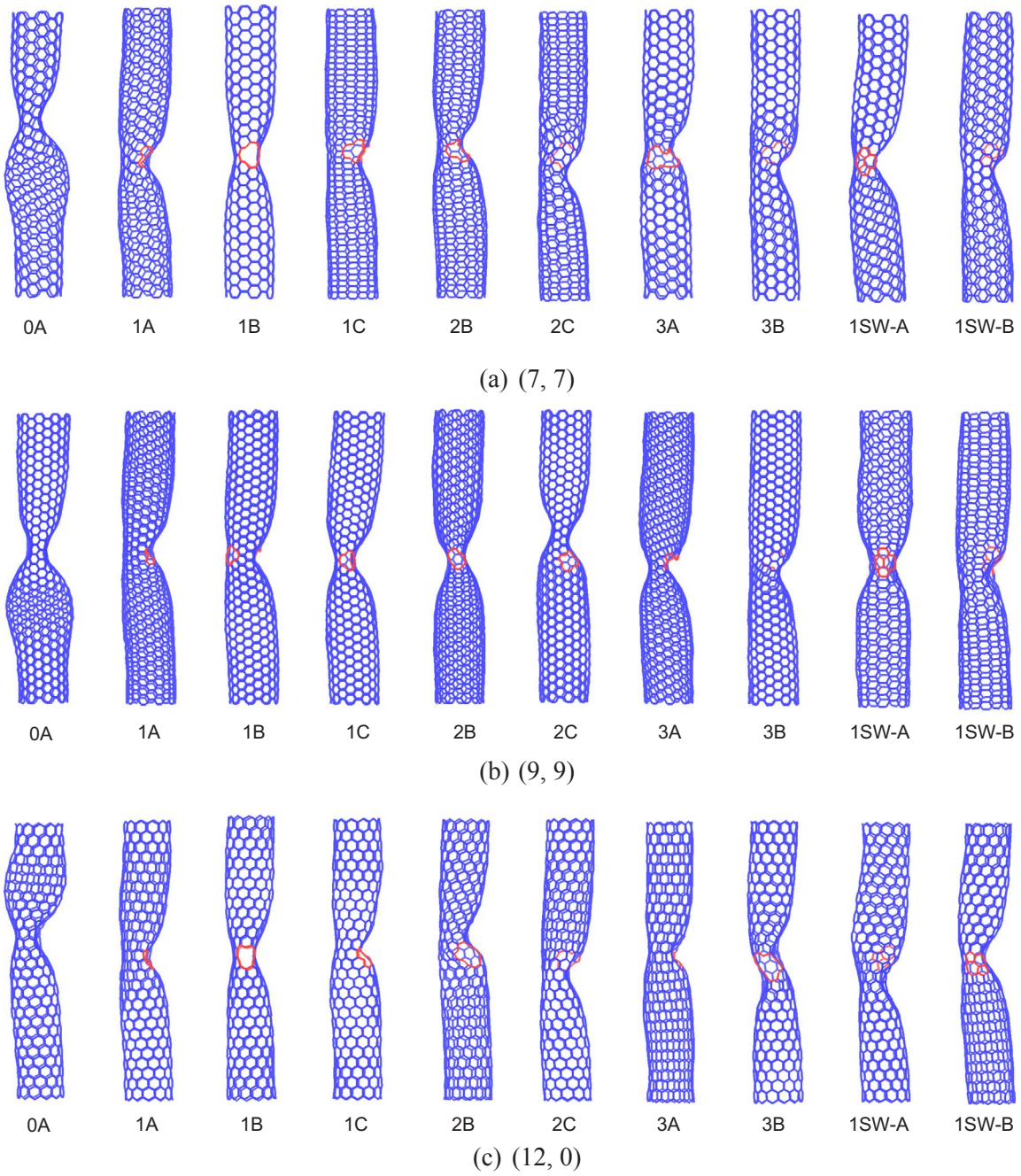

Fig. 8. Buckling mode shapes of the embedded SWCNTs (a), (7, 7), (b) (9, 9) and (c) (12, 0).

4. Conclusions

We conducted a comprehensive molecular dynamics study of the degradation of buckling resistance due to the presence of various types of defects (vacancy and SW defect). In this highly original study, both freestanding and embedded SWCNTs with different sizes and chiralities ((7, 7), (9, 9), and (12, 0)) were investigated, and the results were compared and assessed. Specifically, we investigated several defect configurations including missing atoms, defect symmetry, and vacancy distribution on buckling load and stiffness. Our findings showed that defects generally have the same effect on the buckling strain of freestanding and embedded SWCNTs. However, compared with those of freestanding SWCNTs, the buckling strain and buckling load of embedded SWCNTs are reduced when SWCNTs are confined in an epoxy matrix. Furthermore, increasing the number of missing atoms generally reduces the buckling load of freestanding SWCNTs. Our work also reveals that increasing the number of missing atoms increases the buckling load of embedded armchair SWCNTs because the compressive force is partly supported by the kinks developed during buckling. Furthermore, the

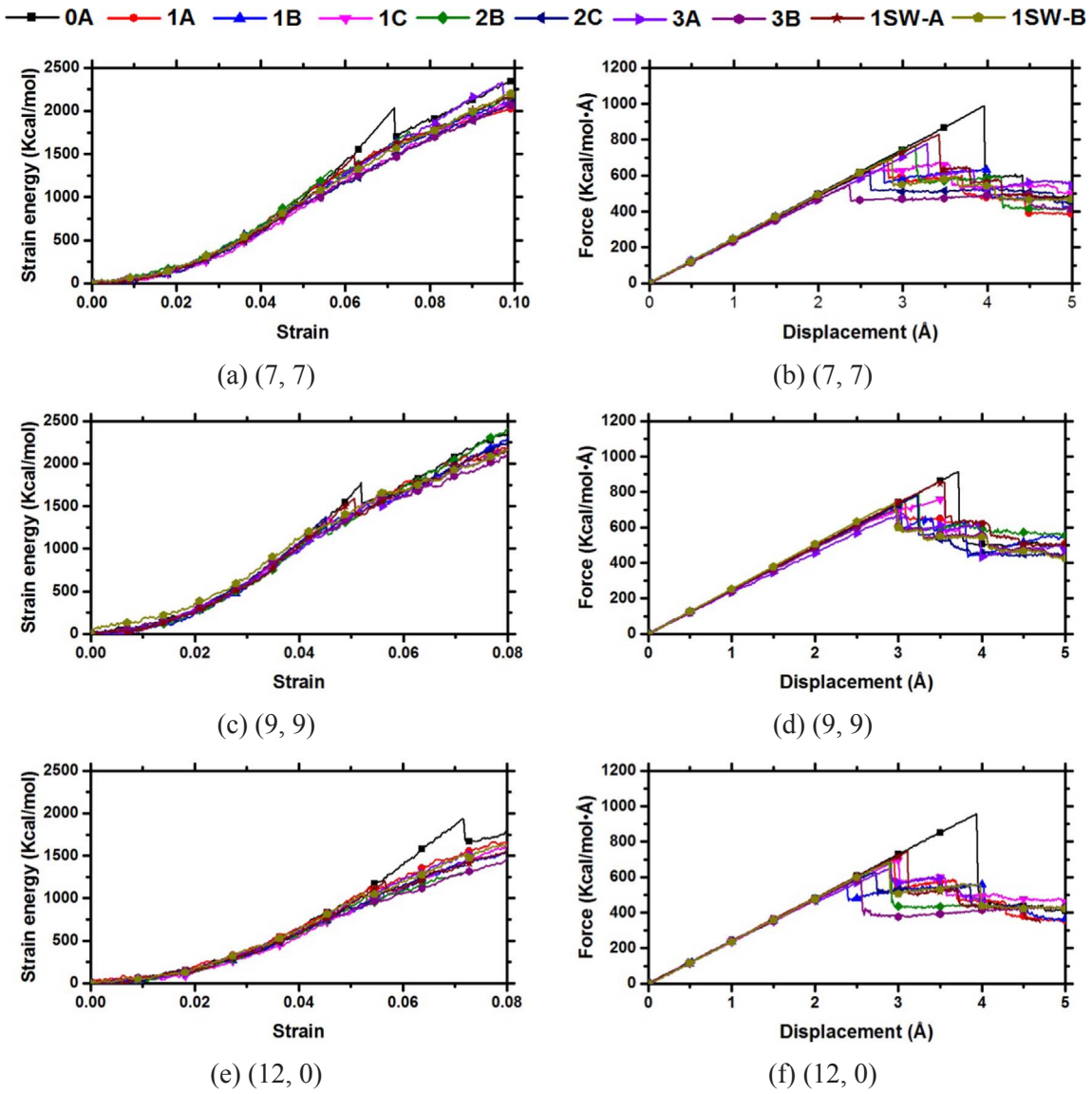

Fig. 9. (a), (c) and (e) Strain energy-strain curves; (b), (d) and (f) force-displacement curves for different embedded defective SWCNTs.

buckling load of freestanding SWCNTs is increased by asymmetric vacancy and SW defects, but the same defects decrease the buckling load of embedded SWCNTs due to the introduction of different buckling modes. Finally, freestanding SWCNTs containing asymmetric vacancy distribution have higher buckling load because of the positions of the kinks relative to the defects, but the opposite is generally true for embedded SWCNTs.

In summary, defects in CNTs are generally unavoidable. Different buckling behaviors involving both freestanding and embedded CNTs containing different defects were distinguished and discussed. Our study clearly shows that we cannot rely on studies focusing only on the buckling of freestanding CNTs when designing CNT-reinforced nanocomposites and that the joint effect of the CNT and the matrix must be considered. It is hoped that the findings of this research would contribute to the design of much improved CNT-reinforced nanocomposites.

Acknowledgements

The financial assistance offered by the Natural Sciences and Engineering Council of Canada (NSERC) and the Discovery Accelerator Supplement is greatly acknowledged by the authors.

References

[1] S. Iijima, Helical microtubules of graphitic carbon, Nature 354 (6348) (1991) 56–58.
[2] Q.H. Wang, A. Setlur, J. Lauerhaas, J. Dai, E. Seelig, R.P. Chang, A nanotube-based field-emission flat panel display, Appl. Phys. Lett. 72 (22) (1998) 2912–2913.
[3] C.A. Cooper, S.R. Cohen, A.H. Barber, H.D. Wagner, Detachment of nanotubes from a polymer matrix, Appl. Phys. Lett. 81 (20) (2002) 3873–3875.
[4] A.H. Barber, S.R. Cohen, H.D. Wagner, Measurement of carbon nanotube–polymer interfacial strength, Appl. Phys. Lett. 82 (23) (2003) 4140–4142.
[5] H. Wagner, O. Lourie, Y. Feldman, R. Tenne, Stress-induced fragmentation of multiwall carbon nanotubes in a polymer matrix, Appl. Phys. Lett. 72 (2) (1998) 188–190.
[6] J.Q. Liu, T. Xiao, K. Liao, P. Wu, Interfacial design of carbon nanotube polymer composites: a hybrid system of noncovalent and covalent functionalizations, Nanotechnology 18 (16) (2007) 165701.
[7] Q.L. Xiong, S.A. Meguid, Atomistic investigation of the interfacial mechanical characteristics of carbon nanotube reinforced epoxy composite, Eur. Polym. J. 69 (2015) 1–15.
[8] J.M. Wernik, S.A. Meguid, Recent developments in multifunctional nanocomposites using carbon nanotubes, Appl. Mech. Rev. 63 (5) (2011) pp. 050801–050801.
[9] M.B. Nardelli, B.I. Yakobson, J. Bernholc, Brittle and ductile behavior in carbon nanotubes, Phys. Rev. Lett. 81 (21) (1998) 4656.
[10] P.G. Collins, Defects and disorder in carbon nanotubes, Oxford Handbook of Nanoscience and Technology: Frontiers and Advances, 2010.
[11] J.-C. Charlier, Defects in carbon nanotubes, Acc. Chem. Res. 35 (12) (2002) 1063–1069.
[12] H. Dai, J.H. Hafner, A.G. Rinzler, D.T. Colbert, R.E. Smalley, Nanotubes as nanoprobes in scanning probe microscopy, Nature 384 (6605) (1996) 147–150.
[13] S. Iijima, C. Brabec, A. Maiti, J. Bernholc, Structural flexibility of carbon nanotubes, J. Chem. Phys. 104 (5) (1996) 2089–2092.
[14] E.W. Wong, P.E. Sheehan, C.M. Lieber, Nanobeam mechanics: elasticity, strength, and toughness of nanorods and nanotubes, Science 277 (5334) (1997) 1971–1975.
[15] O. Lourie, D. Cox, H. Wagner, Buckling and collapse of embedded carbon nanotubes, Phys. Rev. Lett. 81 (8) (1998) 1638.
[16] L. Schadler, S. Giannaris, P. Ajayan, Load transfer in carbon nanotube epoxy composites, Appl. Phys. Lett. 73 (26) (1998) 3842–3844.
[17] B.I. Yakobson, C.J. Brabec, J. Bernholc, Nanomechanics of carbon tubes: instabilities beyond linear response, Phys. Rev. Lett. 76 (14) (1996) 2511–2514.
[18] C. Ru, Effect of van der Waals forces on axial buckling of a double-walled carbon nanotube, J. Appl. Phys. 87 (10) (2000) 7227–7231.
[19] C.Y. Wang, C.Q. Ru, A. Mioduchowski, Axially compressed buckling of pressured multiwall carbon nanotubes, Int. J. Solids Struct. 40 (15) (2003) 3893–3911.
[20] J.M. Wernik, S.A. Meguid, Coupling atomistics and continuum in solids: status, prospects, and challenges, Int. J. Mech. Mater. Des. 5 (1) (2009) 79–110.
[21] Y.Y. Zhang, C.M. Wang, V.B.C. Tan, Buckling of carbon nanotubes at high temperatures, Nanotechnology 20 (21) (2009).
[22] K. Talukdar, R. Agrawala, A.K. Mitra, Dependence of mechanical characteristics and the fracture and buckling behavior of single-walled carbon nanotubes on their geometry, New Carbon Mater. 26 (6) (2011) 408–416.
[23] B. Motevalli, A. Montazeri, J.Z. Liu, H. Rafii-Tabar, Comparison of continuum-based and atomistic-based modeling of axial buckling of carbon nanotubes subject to hydrostatic pressure, Comput. Mater. Sci. 79 (2013) 619–626.
[24] C. Wang, A.R. Chowdhury, S. Koh, Y. Zhang, Molecular dynamics simulation and continuum shell model for buckling analysis of carbon nanotubes, Modeling of Carbon Nanotubes, Graphene and their Composites, Springer International Publishing, 2014, pp. 239–273.
[25] Y.Y. Zhang, C.M. Wang, V.B.C. Tan, Buckling of multiwalled carbon nanotubes using Timoshenko beam theory, J. Eng. Mech. 132 (9) (2006) 952–958.
[26] S.P. Timoshenko, J.M. Gere, Theory of Elastic Stability, McGraw-Hill Book Company, New York, 1961.
[27] C. Ru, Axially compressed buckling of a double walled carbon nanotube embedded in an elastic medium, J. Mech. Phys. Solids 49 (6) (2001) 1265–1279.
[28] S. Kitipornchai, X. He, K. Liew, Buckling analysis of triple-walled carbon nanotubes embedded in an elastic matrix, J. Appl. Phys. 97 (11) (2005) 114318.
[29] K.M. Liew, X.Q. He, S. Kitipornchai, Buckling characteristics of embedded multi-walled carbon nanotubes, Proc. R. Soc. A – Math. Phys. Eng. Sci. 461 (2064) (2005) 3785–3805.
[30] N. Chandra, S. Namilae, Tensile and compressive behavior of carbon nanotubes: effect of functionalization and topological defects, Mech. Adv. Mater. Struct. 13 (2) (2006) 115–127.
[31] H. Xin, Q. Han, X.-H. Yao, Buckling and axially compressive properties of perfect and defective single-walled carbon nanotubes, Carbon 45 (13) (2007) 2486–2495.
[32] X. Hao, H. Qiang, X. Yao, Buckling of defective single-walled and double-walled carbon nanotubes under axial compression by molecular dynamics simulation, Compos. Sci. Technol. 68 (7–8) (2008) 1809–1814.
[33] Y.Y. Zhang, Y. Xiang, C.M. Wang, Buckling of defective carbon nanotubes, J. Appl. Phys. 106 (11) (2009).
[34] D.D.T.K. Kulathunga, K.K. Ang, J.N. Reddy, Molecular dynamics analysis on buckling of defective carbon nanotubes, J. Phys. Condens. Matter 22 (34) (2010).
[35] A.R. Ranjbartoreh, G. Wang, Effect of topological defects on buckling behavior of single-walled carbon nanotube, Nanoscale Res. Lett. 6 (2011).
[36] V. Parvaneh, M. Shariati, A.M.M. Sabed, Investigation of vacancy defects effects on the buckling behavior of SWCNTs via a structural mechanics approach, Eur. J. Mech. A – Solids 28 (6) (2009) 1072–1078.
[37] R.H. Poelma, H. Sadeghian, S. Koh, G.Q. Zhang, Effects of single vacancy defect position on the stability of carbon nanotubes, Microelectron. Reliab. 52 (7) (2012) 1279–1284.
[38] Q. Cheng, X.X. Wang, N.G. Ni, Molecular dynamics simulation for compressive mechanics properties of SWCNT with random distributed vacancies, in: C. Bai, S. Xie, X. Zhu (Eds.), Nanoscience and Technology, Pts 1 and 2, 2007, pp. 1161–1164.
[39] S. Namilae, N. Chandra, Role of atomic scale interfaces in the compressive behavior of carbon nanotubes in composites, Compos. Sci. Technol. 66 (13) (2006) 2030–2038.
[40] D.D.T.K. Kulathunga, K.K. Ang, Modeling and simulation of buckling of embedded carbon nanotubes, Comput. Mater. Sci. 81 (2014) 233–238.
[41] S. Plimpton, Fast parallel algorithms for short-range molecular dynamics, J. Comput. Phys. 117 (1) (1995) 1–19.
[42] P. Dauber-Osguthorpe, V.A. Roberts, D.J. Osguthorpe, J. Wolff, M. Genest, A.T. Hagler, Structure and energetics of ligand binding to proteins: Escherichia coli dihydrofolate reductase-trimethoprim, a drug-receptor system, Proteins: Struct. Funct. Bioinf. 4 (1) (1988) 31–47.
[43] A. Alian, S. Kundalwal, S. Meguid, Interfacial and mechanical properties of epoxy nanocomposites using different multiscale modeling schemes, Compos. Struct. 131 (2015) 545–555.
[44] A. Alian, S. Kundalwal, S. Meguid, Multiscale modeling of carbon nanotube epoxy composites, Polymer 70 (2015) 149–160.
[45] A. Kumar, V. Sundararaghavan, A.R. Browning, Study of temperature dependence of thermal conductivity in cross-linked epoxies using molecular dynamics simulations with long range interactions, Modell. Simul. Mater. Sci. Eng. 22 (2) (2014) 025013.
[46] C. Li, G.A. Medvedev, E.-W. Lee, J. Kim, J.M. Caruthers, A. Strachan, Molecular dynamics simulations and experimental studies of the thermomechanical response of an epoxy thermoset polymer, Polymer 53 (19) (2012) 4222–4230.
[47] Q. Wang, V.K. Varadan, Y. Xiang, Q.K. Han, B.C. Wen, On instability of single-walled carbon nanotubes with a vacancy defect, Int. J. Struct. Stab. Dyn. 8 (2) (2008) 357–366.
[48] L. Martínez, R. Andrade, E.G. Birgin, J.M. Martínez, PACKMOL: a package for building initial configurations for molecular dynamics simulations, J. Comput. Chem. 30 (13) (2009) 2157–2164.
[49] W. Humphrey, A. Dalke, K. Schulten, VMD: visual molecular dynamics, J. Mol. Graph. 14 (1) (1996) 33–38.
[50] C. Wang, Y. Zhang, Y. Xiang, J. Reddy, Recent studies on buckling of carbon nanotubes, Appl. Mech. Rev. 63 (3) (2010) 030804.
[51] Y. Zhang, C. Wang, W. Duan, Y. Xiang, Z. Zong, Assessment of continuum mechanics models in predicting buckling strains of single-walled carbon nanotubes, Nanotechnology 20 (39) (2009) 395707.
[52] Y. Zhang, V. Tan, C. Wang, Effect of chirality on buckling behavior of single-walled carbon nanotubes, J. Appl. Phys. 100 (7) (2006) 074304.